ARMA 19–1717

Global vs Local Strain Measurements in Triaxial Tests – Implications

Perbawa, A. Gramajo, E. Finkbeiner, T. and Santamarina, J. C.

King Abdullah University of Science and Technology, Thuwal, Makkah, Saudi Arabia

ABSTRACT: Accurate stress-strain measurements in triaxial compression tests are critical to derive correct values of stiffness, Poisson's ratio, and the Biot α-parameter. Yet, inherent biases can produce unrepresentative rock properties. This study investigates the impact of different measurements using strain gauges and LVDTs. A detailed analysis reveals the impact of surface compliance at the interfaces between the specimen and end caps. Tested materials include: standard aluminum, Eagle Ford shale, Berea sandstone, and Jubaila carbonate. Results reveal: 1) Contact deformation adds non-linear behavior to the stress-strain response. 2) Seating effects lower the stiffness computed from cap-to-cap deformation measurements. 3) Strain gauges do not show hysteresis evident in cap-to-cap LVDT systems. 4) Bending due to uneven surfaces and misalignment affect cap-to-cap deformation measurements. 5) Confining pressures improve the contact at the interface and reduce partial slippage. 6) Mounting strain gauges on sleeves is ill-advised. 7) The dynamic modulus is higher than the static modulus. 8) The static and dynamic moduli are sensitive to the imposed axial deviatoric stresses. 9) The estimation of the Biot α-parameter is affected by seating effects. We conclude that specimen–bonded strain gauges are preferred to minimize and possibly avoid any of the above effects for pre-peak strain measurements.

1. INTRODUCTION

Strain measurements are critical for the accurate calculation of stiffness, Poisson's ratio, and Biot α-parameter. These values are used in analyses and designs in the geotechnical, petroleum and mining sectors. Inherent biases within triaxial tests can obscure and distort measured values and produce unrepresentative rock properties (Dendani et al., 1988).

Measurements using cap-to-cap deformation sensors include seating effects due to the mismatch between the specimen and end caps and non-uniform strains along with the specimen due to restrains at the interface (Baldi et al., 1988). Furthermore, studies which compare static and dynamic moduli often reveal large differences, aggravated at low-stress due to the presence of open discontinuities (Cheng, 1981; Fjaer, 1999; Simmons & Brace, 1965; van Heerden, 1987).

In this study, we conduct axial compression tests with intact cylindrical specimens to compare stress-strain measurements obtained with strain gauges mounted directly on specimens against strains computed from deformation measurements with cap-to-cap and local LVDTs. We use these results to quantitatively address and understand discrepancies in estimated moduli obtained from local and global measurements. On that note, we include a complete experimental dataset and a comprehensive analysis of the different possible errors in rock mechanical measurements.

2. PREVIOUS STUDIES

Local measurements avoid unwanted deformations at the interface between the specimen and end caps. Local measurement sensors and methods include: electro level inclinometer (Jardine et al., 1985; Symes and Burland, 1984), Hall effect (Clayton and Khatrush, 1986), digital image processing (Bhandari, et al., 2012; Macari, et al., 1997; Li, et al., 2016; Parker, 1987), local deformation transducer - LDT (Tatsuoka, 1988), proximity sensors (Hird and Yung, 1989), and fiber Bragg grating - FBG (Xu, 2017). The stiffness computed with local deformation measurements is 15% to 45% higher than the stiffness from cap-to-cap measurements (Isah et al., 2018; Yimsiri et al., 2005; Kung, 2007; Xu et al., 2014; Xu, 2017; Kumar et al., 2016).

3. EXPERIMENTAL STUDIES

This paper investigates differences between global and local measurements and underlying seating effects. The experimental study consists of three parts.

3.1. Part I

The first experimental study involves a standard aluminum specimen (Table 1). We monitor triaxial compression tests using strain gauges, LVDTs, and ultrasonic wave velocities.

Table 1. Specimen specifications, confining pressures and peak stresses used during the loading/unloading cycles.

Specimen	Length [mm]**	Diameter [mm]**	L:D ratio	Mass [gr]***	Estimated UCS [MPa]	Confining Pressure [MPa]	Peak Stress [MPa] 1st cycle	2nd cycle	3rd cycle
Aluminum	50.230	25.105	2.00:1	67.132	~289*	0, 10, 30, 60	60	60	60
Eagle Ford Shale	50.896	25.435	2.00:1	65.639	130-150	0	58	58	58
Berea Sandstone	51.349	25.385	2.02:1	55.194	62-78	0	35	35	-
Jubaila Carbonate 1	57.841	26.813	2.16:1	78.752	24-48	0	21	21	-
Jubaila Carbonate 2	53.953	26.714	2.02:1	72.989	24-48	0	10	15	20

Note: *(ASTM B211, 2012) **Uncertainty in length and diameter are 5 µm. *** Uncertainty in mass is 0.5 mg.
The average top and bottom surface roughness for the rock samples is ~10 µm.

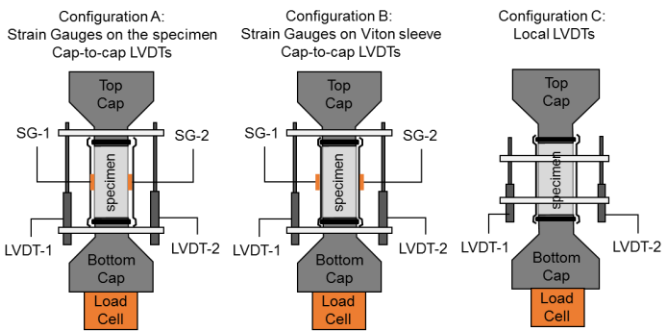

Fig. 1. Experimental setups. Configuration A: two strain gauges mounted directly on the specimen. Configuration B: two strain gauges bonded on top of the protective Viton sleeve. In both configurations, the strain gauges are aligned parallel to cap-to-cap LVDTs. Configuration C: two local LVDTs mounted within the specimen height and on top of the Viton sleeve.

We mount two strain gauges opposite to each other at the mid-height of the sample, and two cap-to-cap LVDTs (Figure. 1). The strain gauges are either linear or rosette type. The rosette gauges have a 3.18 mm length with a $\pm 3x10^{-2}$ strain range and 10^{-6} strain resolution and allow collecting axial and radial strain data simultaneously for the accurate determination of Poisson's ratio. The linear gauges are 3.18 and 12.7 mm long with a $\pm 3x10^{-2}$ strain range. The installation of strain gauges follows ASTM standard procedures (ASTM-D2166, 2016; ASTM-D3148, 2002; ASTM-D4767, 2011; ASTM-D7181, 2011). We test two different mounting types: in Configuration A gauges are attached directly to the specimen, and in Configuration B gauges are bonded onto the Viton Sleeve. We also examine two installations for the LVDTs: cap-to-cap (Configuration A and B) and local (Configuration C).

The loading sequence involves: (1) three loading/unloading cycles to 40 MPa at different strain rates (Figure. 2); and (2) three loading/unloading cycles to 60 MPa. We repeated the test at four confining stress levels: 0 MPa (unconfined), 10 MPa, 30 MPa and finally 60 MPa. The selection of confining pressure reflects variations of in-situ confinement commonly modeled in our studies. The various test sequences are typical for numerous industry and academic applications. We investigate the effect of consecutive axial loading/unloading cycles on both seating effects and stiffness and the relationship between seating effects and axial deviatoric stress.

3.2. *Part II*

The second experimental study explores the impact of seating effects by re-polishing the specimen ends (ASTM-D4543, 2008). We use the same aluminum standard previously described. We scan the original and polished surfaces of the specimen and end caps using the NANOVEA optical profilometer Jr25 (lateral resolution of 14 µm and vertical resolution of 0.5 µm).

3.3. *Part III*

We extend the experimental study to rock specimens using the same test protocols described above. We test Lower Eagle Ford shale (Western Gulf outcrop belt, Texas, USA), the late Upper Jurassic Jubaila carbonate (Riyadh outcrop, Saudi Arabia), and Berea sandstone. However, this paper only present data from Eagle Ford shale specimen. Table 1 shows specimen dimensions, axial stresses, and confining pressures. In addition to the local strain and global deformation measurements, we acquire ultrasonic transit times for all samples during loading/unloading cycles taken every 1 MPa of axial load increment.

4. EXPERIMENTAL RESULTS

4.1. *Local strain vs. global deformation: Seating effects (aluminum specimen)*

The strain rates $\dot{\varepsilon}_z = 0.5x10^{-6}\, s^{-1}$, $10^{-6}\, s^{-1}$ and $2x10^{-6}\, s^{-1}$ does not affect the Young's modulus (Figure 2). The stress-strain curve using cap-to-cap LVDT shows hysteresis and the computed stiffness is E ≈ 59 GPa. This value is markedly below the stiffness obtained from the strain gauges, which agrees with the reference Young's modulus for aluminum E ≈ 69 GPa (Callister and Rethwisch, 2007 - Figure 2). Lower values of axial deviatoric stress reveal more pronounced non-linear stress-strain behavior when using cap-to-cap LVDT deformation measurements.

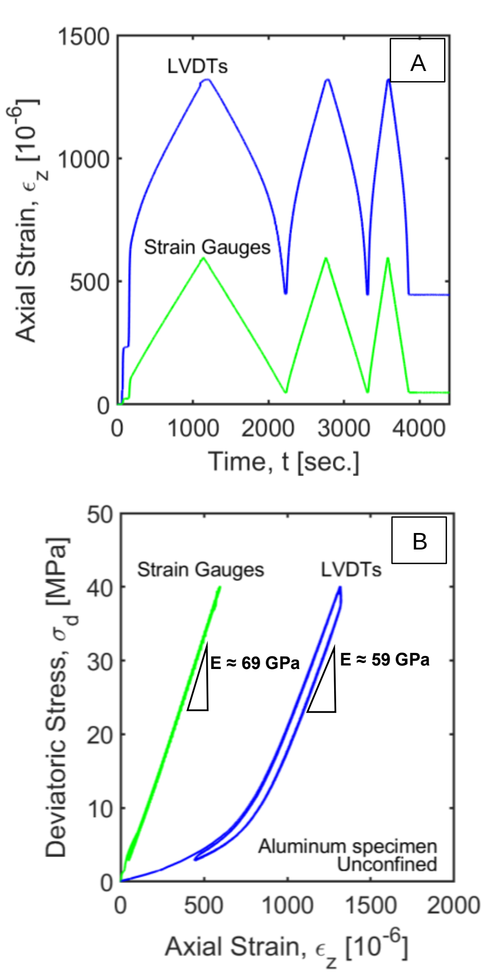

Fig. 2. (A) Loading sequence. (B) Stress-strain curves for unpolished aluminum specimen. Green line: strain measurement with gauges. Blue line: strain computed from cap-to-cap LVDT measurements. Both stress-strain curves follow the same loading unloading paths, regardless of the different strain rates.

We observe seating effects on polished and original rough specimens. Data gathered with the polished aluminum specimen show small seating effects up to an axial strain of ~10^{-4} and axial deviatoric stress of ~5 MPa (Figure 3a). By contrast, the original rougher surfaces show seating effects up to an axial strain of ~$7x10^{-4}$ and axial deviatoric stress of ~17 MPa (Figure 3b).

Seating effects and hysteresis are avoided when using strain gauges bonded on the specimen (Figure 3a). The Young's modulus derived from cap-to-cap LVDTs is 8.5% lower than from strain gauges even for the polished specimen. Clearly, seating effects have a marked effect on the stress-strain curve.

4.2. *Bending effect (aluminum specimen)*

Specimen bending is particularly noticeable in cap-to-cap LVDT data during unconfined tests (Figure 3). Computed strain from LVDT-1 deformation measurement is higher than LVDT-2. In contrast, measured strains from the two gauges (SG-1 and SG-2 green lines) plot on top of each other. Therefore, using only one single LVDT would lead to biased results.

4.3. *Gauge slippage (aluminum specimen)*

The Viton sleeve does not always follow the deformation of the specimen during loading/unloading cycles, as the sleeve may slip along the specimen surface. Then, strain values measured using gauges mounted on the sleeve will be smaller than the specimen strain leading to unreasonably high stiffness (Figure 3b: the estimated Young's modulus E ≈ 419 GPa is six times higher than

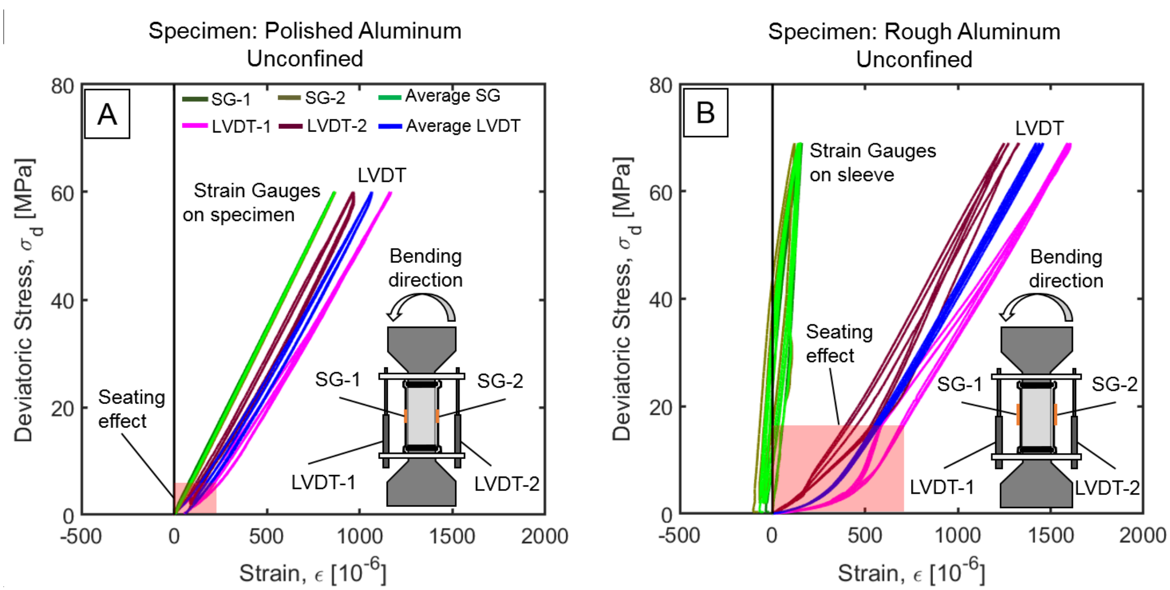

Fig. 3. Measured deformation between two opposite LVDTs and local strains from opposite strain gauges (SG). (A) Strain gauges mounted directly on the specimen. (B) Strain gauges mounted on the Viton sleeve. Green line: average strain measurement with gauges. Blue line: average strain computed from cap-to-cap LVDT measurements. Aluminum specimen polished (left) and original rough (right). Pink box: seating effects (non-linear behavior).

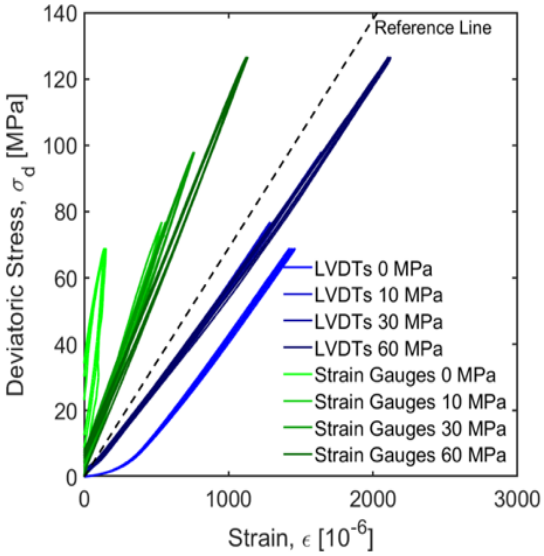

Fig. 4. Effect of confining pressure on seating effects on aluminum specimen. Strain gauges mounted on the Viton sleeve and cap-to-cap LVDTs. Green line: average strain measurement with gauges. Blue line: average strain computed from cap-to-cap LVDT measurements. Darker green or blue lines correspond to higher confining pressures. Dashed black reference line: equivalent to standard aluminum Young's modulus E = 69 GPa.

the standard value of E = 69 GPa). Higher confining pressure hinders sleeve-specimen slip (Figure 4). Nevertheless, mounting even long strain gauges on top of the sleeves is ill-advised.

Strain gauges fixed directly on the specimen prevent slippage but require properly sealed cables to avoid leakage. In our setup, we pierce a small hole through the Viton sleeve directly at the location where the cables attach to the gauges and fill the hole with both silicon sealant and polyurethane.

4.4. *Confining pressure (aluminum specimen)*

Confining pressure improves the contact between the specimen and end caps and reduces seating effects (Figure 4 – Table 2).

Table 2. Effect of confining pressure on estimated Young's modulus for aluminum specimen.

Confining Pressure	Young's Modulus [GPa] Polished LVDTs	Polished Strain Gauges*	Original rough LVDTs	Original rough Strain Gauges**
0 MPa	62.95	69.89	59.99	419.47
10 MPa	63.50	69.58	59.66	137.28
30 MPa	63.87	69.39	58.69	122.29
60 MPa	63.81	68.91	58.43	106.21

Note: *Bonded on specimen. ** Mounted on Viton sleeve.

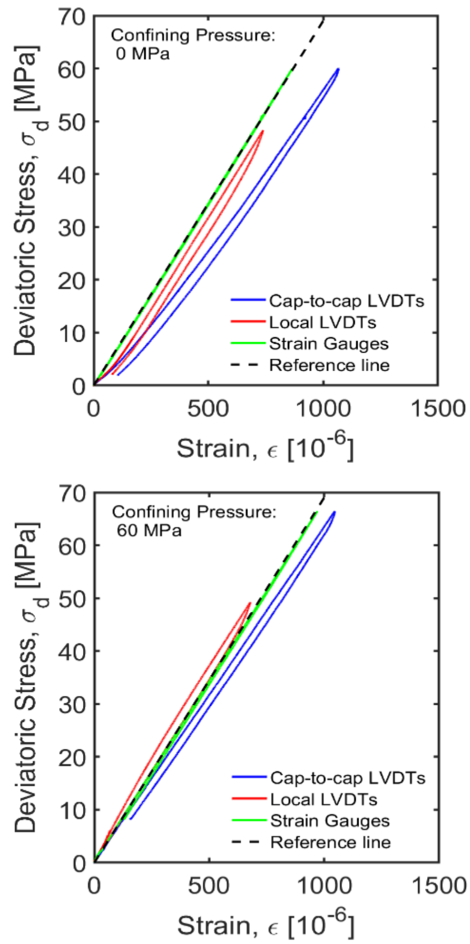

Fig. 5. Aluminum stress-strain curves. Green line: average strain measurement with gauges. Blue line: average strain computed from cap-to-cap LVDT measurements. Red line: average strain computed from local LVDTs. Test at 0 MPa (top figure) and 60 MPa (bottom figure) confining pressure. Dashed black reference line: equivalent to standard aluminum Young's modulus E = 69 GPa.

4.5. *Local LVDTs (aluminum specimen)*

We also investigate the benefit of mounting LVDTs on the specimen mid-height with a separation of 26 mm between clamps (Configuration C – Figure 1). The local LVDT system shows an improved Young's modulus E = 69 GPa. However, the local LVDTs still show hysteresis probably because of sleeve slippage underneath the clamps. Therefore, specimen–bonded strain gauges are the best option for pre-peak strain measurements (Figure 5).

4.6. *Surface roughness (aluminum specimen)*

The unpolished specimen surface is approximately concave in shape with its circumferential ring ~80 μm higher than the center (Figure 6a). The polished specimen has a 10 μm initial roughness (Figure 7). For comparison,

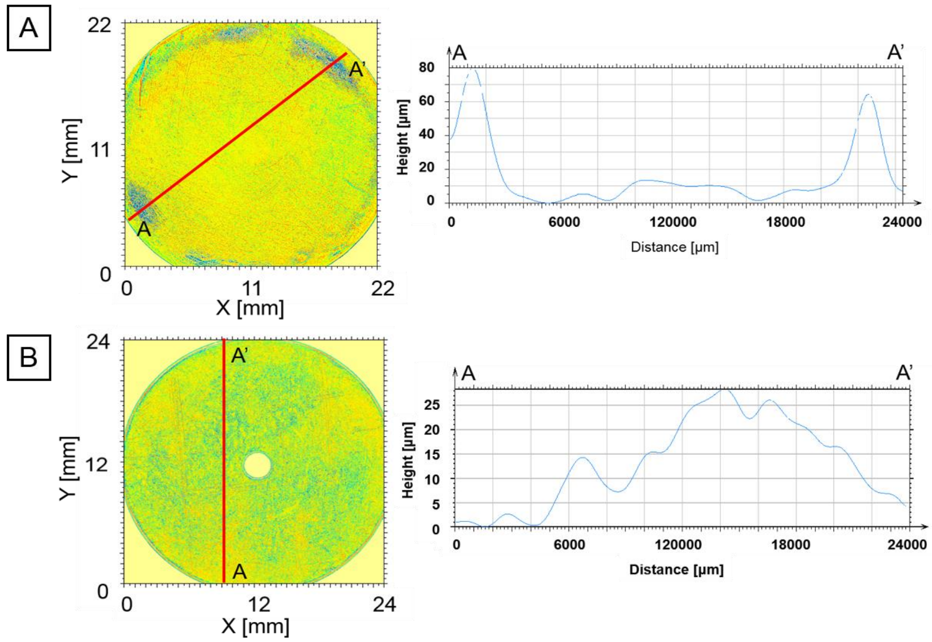

Fig. 6. Surface topography of the (A) original aluminum specimen surface, and (B) instrument end cap. These plots display elevation gathered with a profilometer. The aluminum surface displays higher topographical values closer to the edge with a height up to 80 µm. By contrast, the end cap shows a convex geometry with a maximum height of ~28 µm.

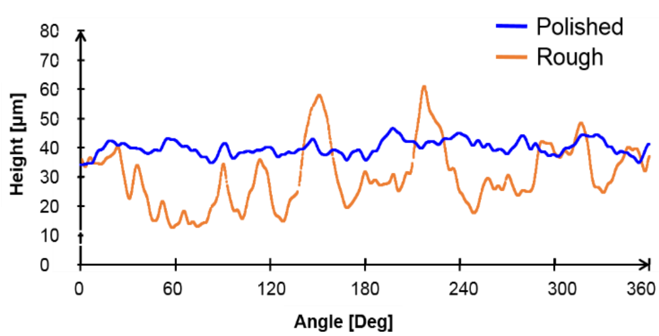

Fig. 7. Surface topography of original rough (orange line) and polished (blue line) aluminum specimen. Data showed along the aluminum specimen circumferential ring, close to the edge.

the ASTM-D4543 prescribes a maximum tolerable surface roughness of 25 µm. Furthermore, the end caps of our testing system have a convex shape with a height variation of ~28 µm (Figure 6b). The unevenness of the end caps causes seating effects even in the polished specimen (Figure 3a). Furthermore, the aluminum specimen end surfaces deform during consecutive tests due to the non-flat end caps.

5. ANALYSES AND DISCUSSION

5.1. *Seating effect*

The total deformation measured by a cap-to-cap LVDT δ_{total} involves three components: the specimen δ_{spec}, end cap δ_{cap}, and the interface δ_{cont}.

$$\delta_{total} = \delta_{spec} + 2\delta_{cap} + 2\delta_{cont} \tag{1}$$

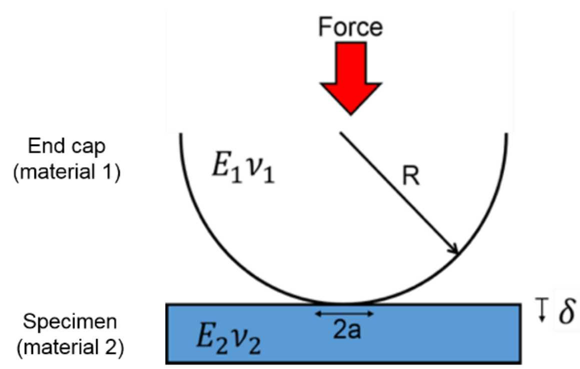

Fig. 8. Seating effect as a Hertzian contact.

where,

$$\delta_{spec} = \frac{F.L_{spec}}{E_{spec}.A_{spec}} \tag{2}$$

$$\delta_{cap} = \frac{F.L_{cap}}{E_{cap}.A_{cap}} \tag{3}$$

Parameters include the specimen length L_{spec}, the cap length to the LVDT's clamp L_{cap}, the applied force F, materials Young's modulus E, and the cross-sectional area A. We analyze seating effects using Hertzian contact theory (Johnson, 1985). We consider a spherical surface in contact with a flat half-space (Note: the underlying assumption is that the majority of the sphere deformation takes place at the contact - Figure 8). The contact deformation δ_{cont} predicted by Hertzian contact theory is

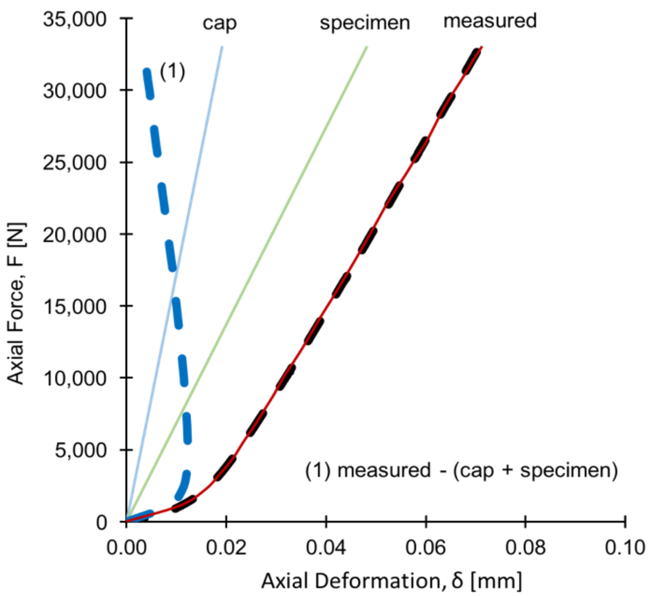

Fig. 9. Deformation components. Green line: Analytical specimen deformation. Solid blue line: Analytical end cap deformation. Dashed black line: Experimental cap-to-cap deformation. Dashed blue line: contact deformation. Red line: Analytical total deformation using the Hertzian contact model.

$$\delta_{cont} = \sqrt[3]{\left(\frac{2F^2}{E_{eff}^2 R}\right)} \tag{4}$$

where R is the spherical radius. From the Pythagorean relation:

$$(R - X)^2 + \left(\frac{D}{2}\right)^2 = R^2 \tag{5}$$

where, X is the profilometer maximum convexity and D the cap diameter. The effective contact stiffness is

$$E_{eff} = \frac{2}{\left(\frac{1 - \nu_1^2}{E_1} + \frac{1 - \nu_2^2}{E_2}\right)} \tag{6}$$

Material 1 corresponds to the Titanium end caps, and material 2 indicates the aluminum specimen.

Figure 9 presents the contribution of the specimen, end caps, and contacts to the total cap-to-cap deformation (parameters listed in Table 3). The cap's deformation provides the smallest contribution (high stiffness and short length). The contact deformation is equal to the experimental cap-to-cap deformation minus the specimen and end caps deformations. The non-linear contact deformation is pronounced in the low force regime.

The values of convexity X that match the total analytical deformation range from X = 14.5 to 50 µm. These results emphasize the importance of using strain gauges (local measurements) since seating effects are still apparent for the most polished specimen surface.

Table 3 Parameters used for Hertzian contact analysis

Parameters	Value	Unit
E_{spec}	69,000	MPa
ν_{spec}	0.33	unitless
L_{spec}	50.23	mm
A_{spec}	494.62	mm^2
E_{cap}	120,000	MPa
ν_{cap}	0.37	unitless
L_{cap}	22.4	mm
A_{cap}	506.71	mm^2
D	25.4	mm

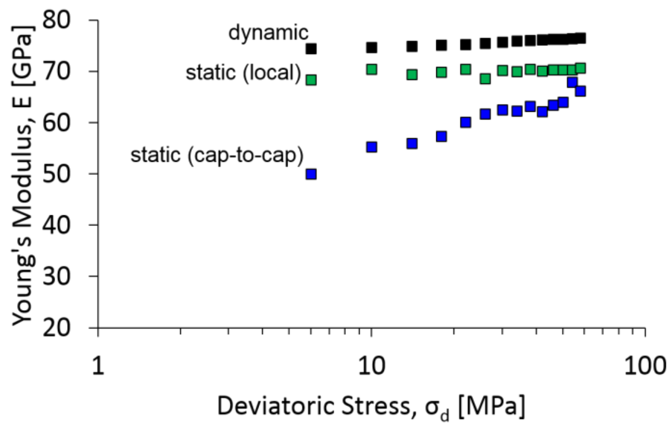

Fig. 10. Quasi-static and dynamic stiffness for the aluminum specimen at 0 MPa confining pressure as a function of deviatoric stress.

5.2. *Seating effects on the static and dynamic Young's moduli*

Figure 10 shows the tangential quasi-static modulus computed every 5 MPa of axial deviatoric stress and the dynamic modulus computed from ultrasonic velocities. The static modulus estimated from cap-to-cap deformations exhibits a higher stress sensitivity due to the non-linear seating effects. The static modulus from local strain measurements and the dynamic modulus follow almost flat lines. The dynamic modulus is higher than the quasi-static modulus due to differences in strain levels and rates.

Figure 11 presents similar results for the dynamic and static moduli of an Eagle Ford shale specimen. Once again, seating effects have a pronounced effect on stiffness determined from cap-to-cap measurements. The stress sensitivity observed for local measurements as compared to dynamic values suggests distinct effects for mineral bonding, layering and global inhomogeneity on quasi-static and acoustic measurements.

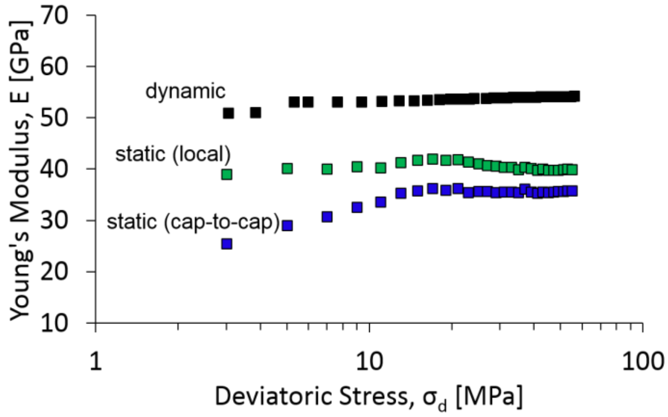

Fig. 11. Quasi-static and dynamic stiffness for the Eagle Ford shale at 0 MPa confining pressure as a function of deviatoric stress.

5.3. *Impact on Biot's α-parameter*

Biot's α-parameter relates the applied total stress σ and pore fluid pressure P_p to the effective stress σ' (Biot, 1941),

$$\sigma' = \sigma - \alpha P_p \tag{7}$$

Biot's α-parameter requires careful measurement of the skeleton K_s and the grain K_m bulk moduli:

$$\alpha = 1 - \frac{K_s}{K_m} \tag{8}$$

Results presented above show that cap-to-cap deformation measurements lead to a lower skeleton bulk modulus K_s due to seating effects and results in higher α-values.

6. CONCLUSIONS

This study investigated seating effects and compared local strain and deformation measurements versus cap-to-cap LVDT systems. Key findings follow: 1) Bending due to uneven surfaces and misalignment affect cap-to-cap deformation measurements. The average values obtained from sensor pairs tend to cancel bending effects. 2) Seating effects lower the stiffness computed from cap-to-cap deformation measurements. 3) Contact deformation adds non-linear behavior to the measured stress-strain response; this is more pronounced at low confinement and axial deviatoric stresses. 4) Hertzian contact guides the analysis of seating effects. 5) Strain gauges do not show hysteresis evident in cap-to-cap LVDT systems. 6) Higher confining pressures improve the contact at the interface and reduce partial slippage between the sample and the sleeve; yet, mounting strain gauges on sleeves is ill-advised. 7) The dynamic modulus is higher than the static modulus (local strain measurements) probably due to differences in strains and strain rates. 8) The static and dynamic moduli are sensitive to the imposed axial deviatoric stresses. 9) The estimation of the Biot α-parameter is affected by seating effects. Ultimately, specimen–bonded strain gauges are preferred to minimize and possibly avoid any of the above effects for pre-peak strain measurements.

7. ACKNOWLEDGEMENTS

Support provided by The KAUST Endowment at King Abdullah University of Science and Technology for this research. Gabrielle E. Abelskamp edited the manuscript.

8. REFERENCES

1. ASTM-B211. (2012). Standard Specification for Aluminum and Aluminum-Alloy Rolled or Cold-Finished Bar , Rod , and Wire. ASTM, 1-10. https://doi.org/10.1520/B0211M-12E01.2

2. ASTM-D2166. (2016). Standard Test Method for Unconfined Compressive Strength of Cohesive Soil. *ASTM*, *i*(January), 1–7. https://doi.org/10.1520/D2166

3. ASTM-D3148. (2002). Standard Test Method for Elastic Moduli of Intact Rock Core Specimens in Uniaxial Compression. *ASTM*, *04*, 1–6. https://doi.org/10.1520/D7012-10.1

4. ASTM-D4543. (2008). Standard Practices for Preparing Rock Core as Cylindrical Test Specimens and verifying Conformance to Dimensional and Shape Tolerances. *ASTM*, 1–9. https://doi.org/10.1520/D4543-08.

5. ASTM-D4767. (2011). Standard Test Method for Consolidated Undrained Triaxial Compression Test for Cohesive Soils. *ASTM*, *i*, 1–11. https://doi.org/10.1520/D4767-11.2

6. ASTM-D7181. (2011). Standard Test Method for Consolidated Drained Triaxial Compression Test for Soils. *ASTM*, (August), 1–11. https://doi.org/10.1520/D7181-11.Copyright

7. ASTM-E111. (1997). Standard Test Method for Young ' s Modulus , Tangent Modulus , and Chord Modulus. *ASTM*, *03*, 1–7. https://doi.org/10.1520/E0111-04R10

8. Baldi, G., Hight, D. W., & Thomas, G. E. (1988). State-of-the-art Paper - A Reevaluation of Conventional Triaxial Test Methods. In *Advanced Triaxial Testing of Soil and Rock - STP 977* (pp. 219–263).

9. Bhandari, A., Powrie, W., & Harkness, R. (2012). A Digital Image-Based Deformation Measurement System for Triaxial Tests. *ASTM Geotechnical Testing*

Journal, *35*(2), 209–226.

10. Biot, M. A. (1941). General theory of three-dimensional consolidation. *Journal of Applied Physics*, *12*(2), 155–164. https://doi.org/10.1063/1.1712886

11. Cheng, C. H. (1981). Dynamic and Static Moduli. *Geophysical Research Letters*, *8*(1), 39–42.

12. Clayton, C. R. I., & Khatrush, S. A. (1986). A new device for measuring local axial strains on triaxial specimens. *Geotechnique*, *36*(4), 593–597.

13. Dendani, H., Flavigny, E., & F, J. J. (1988). Triaxial Test for Embankment Dams: Interpretation and Validity. In *Advanced Triaxial Testing of Soil and Rock* (pp. 486–500). Phiadelphia: ASTM.

14. Fjaer, E. (1999). Static and dynamic moduli of weak sandstones. In *Rock Mechanics for Industry* (pp. 675–681). American Rock Mechanics Association.

15. Gautam, K. (2003). *Fluid Effects on attenuation and dispersion of elastic waves*. *Colorado School of Mines*. Colorado School of Mines.

16. Hird, C. C., & Yung, P. C. Y. (1989). Use of proximity transducers for local strain measurements in triaxial tests. *Geotechnical Testing Journal*, *12*(4), 292–296.

17. Isah, B. W., Mohamad, H., & Harahap, I. S. H. (2018). International Journal of Advanced and Applied Sciences Measurement of small-strain stiffness of soil in a triaxial setup : Review of local instrumentation. *International Journal of Advanced and Applied Sciences*, *5*(7), 15–26. https://doi.org/10.21833/ijaas.2018.07.003

18. Jardine, R. J., Symes, N. J., & Burland, J. B. (1985). Discussion: The measurement of soil stiffness in the triaxial apparatus. *Géotechnique*, *35*(3), 378–382. https://doi.org/10.1680/geot.1985.35.3.378

19. Johnson, K. L. (1985). *Contact Mechanics*. Cambridge University Press.

20. Kumar, S. S., Khrisna, A. M., & Dey, A. (2016). Local Strain Measurements in Triaxial Tests Using on - Sample Transducers. In *Indian Geotechnical Conference IGC2016* (pp. 1–4).

21. Kung, G. T. C. (2007). Equipment and testing procedures for small strain triaxial tests. *Journal of the Chinese Institute of Engineers, Transactions of the Chinese Institute of Engineers,Series A/Chung-Kuo Kung Ch'eng Hsuch K'an*, *30*(4), 579–591. https://doi.org/10.1080/02533839.2007.9671287

22. Li, L., Zhang, X., Chen, G., & Lytton, R. (2016). Measuring unsaturated soil deformations during triaxial testing using a photogrammetry-based method. *Canadian Geotechnical Journal*, *53*(3), 472–489. https://doi.org/10.1046/j.1365-2850.2000.00333.x

23. Macari, E. J., Parker, J. K., & Costes, N. C. (1997). Measurement of Volume Changes in Triaxial Tests Using Digital Imaging Techniques. *Geotechnical Testing Journal*, *20*(1), 103. https://doi.org/10.1520/GTJ11424J

24. Parker, J. K. (1987). Image Processing and Analysis for the Mechanics of Granular Materials Experiment. In *ASME Proceedings of the 19th SE Symposium on System Theory*.

25. Simmons, G., & Brace, W. F. (1965). Comparison of static and dynamic measurements of compressibility of rocks. *Journal of Geophysical Research*, *70*(22), 5649–5656. https://doi.org/10.1029/JZ070i022p05649

26. Symes, M., & Burland, J. (1984). Determination of Local Displacements on Soil Samples. *Geotechnical Testing Journal*, *7*(2), 49. https://doi.org/10.1520/GTJ10593J

27. Tatsuoka, F. (1988). Some Recent Developments in Triaxial Testing Systems for Cohesionless Soils. In R. T. Donaghe, R. C. Chaney, & M. L. Silver (Eds.), *Advanced Triaxial Testing of Soil and Rock* (pp. 7–67). Phiadelphia: ASTM.

28. van Heerden, W. L. (1987). General relations between static and dynamic moduli of rocks. *International Journal of Rock Mechanics and Mining Sciences and Geomechanics*, *24*(6), 381–385. https://doi.org/10.1016/0148-9062(87)92262-5

29. Xu, D. S. (2017). A new measurement approach for small deformations of soil specimens using fiber bragg grating sensors. *Sensors (Switzerland)*, *17*(1016), 1–13. https://doi.org/10.3390/s17051016

30. Xu, D. S., Borana, L., & Yin, J. H. (2014). Measurement of small strain behavior of a local soil by fiber Bragg grating-based local displacement transducers. *Acta Geotechnica*, *9*(6), 935–943. https://doi.org/10.1007/s11440-013-0267-y

31. Yimsiri, S., Soga, K., & Chandler, S. G. (2005). Cantilever-type local deformation transducer for local axial strain measurement in triaxial test. *Geotechnical Testing Journal*, *28*(5), 445–451. https://doi.org/10.1520/GTJ11432